

# Supporting Information

## Efficient Cocatalyst-Free Piezo-Photocatalytic Hydrogen Evolution of Defective BaTiO<sub>3x</sub> Nanoparticles from Seawater

Yue Jiang<sup>1\*</sup>, Cui Ying Toe<sup>2</sup>, Sajjad S. Mofarah<sup>1</sup>, Claudio Cazorla<sup>3</sup>, Shery L.Y. Chang<sup>1,5</sup>, Yanting Yin<sup>4</sup>, Qi Zhang<sup>1</sup>, Sean Lim<sup>5</sup>, Yin Yao<sup>5</sup>, Ruoming Tian<sup>5</sup>, Yuan Wang<sup>6</sup>, Tasmia Zaman<sup>1</sup>, Hamidreza Arandiyani<sup>6,7</sup>, Gunther G. Andersson<sup>4</sup>, Jason Scott<sup>2</sup>, Pramod Koshy<sup>1</sup>, Danyang Wang<sup>1\*</sup> and Charles C. Sorrell<sup>1\*</sup>

- <sup>1</sup> School of Materials Science and Engineering, UNSW Sydney, Sydney, NSW 2052, Australia
- <sup>2</sup> Particles and Catalysis Research Group, School of Chemical Engineering, UNSW Sydney, Sydney, NSW 2052, Australia
- <sup>3</sup> Departament de Física, Universitat Politècnica de Catalunya, Campus Nord B4-B5, Barcelona 08034, Spain.
- <sup>4</sup> Flinders Institute for Nanoscale Science and Technology, Flinders University, Adelaide, South Australia 5042, Australia
- <sup>5</sup> Electron Microscope Unit, Mark Wainwright Analytical Centre, UNSW Sydney, Sydney, NSW 2052, Australia
- <sup>6</sup> Centre for Advanced Materials and Industrial Chemistry (CAMIC), RMIT University, Melbourne, VIC 3000, Australia
- <sup>7</sup> Laboratory of Advanced Catalysis for Sustainability, School of Chemistry, University of Sydney, Sydney, NSW 2006, Australia

\*Corresponding authors:

[yue.jiang2@unsw.edu.au](mailto:yue.jiang2@unsw.edu.au); [dy.wang@unsw.edu.au](mailto:dy.wang@unsw.edu.au); [c.sorrell@unsw.edu.au](mailto:c.sorrell@unsw.edu.au)

Number of Pages: 23

Number of Figures: 11

Number of Tables: 5

**Table S1.** Representative summary of investigations of photocatalytic hydrogen production from seawater

Catalyst	Seawater Type	Sample Form	Light Source	Sacrificial Agent	Co-Catalyst	H <sub>2</sub> Production Rate by GC (μmol/g/h)	Ref.
TiO <sub>2</sub> (P25)	Simulated seawater	Nanopowder	UV light	--	CuO	3	[1]
TiO <sub>2</sub> -CdS	Simulated seawater	Nanocomposite	Visible light	Na <sub>2</sub> S + Na <sub>2</sub> SO <sub>3</sub>	Pt	457	[2]
La <sub>2</sub> Ti <sub>2</sub> O <sub>7</sub>	Natural seawater	Nanopowder	UV light	--	NiO, Ni	696	[3]
Cd <sub>x</sub> Zn <sub>1-x</sub> Se	Simulated seawater	Nanopowder	AM 1.5	Na <sub>2</sub> S + Na <sub>2</sub> SO <sub>3</sub>	CoP	36,600	[4]
ZnS <sub>1-x-0.5y</sub> O <sub>x</sub> (OH) <sub>y</sub> -ZnO	Simulated seawater	Nanocomposite	Visible light	Na <sub>2</sub> S + Na <sub>2</sub> SO <sub>3</sub>	--	183	[5]
CdS	Natural seawater	Nanopowder	Visible light	Lactic acid	Carbon dots	4,640	[6]
(Ga <sub>1-x</sub> Zn <sub>x</sub> )(N <sub>1-x</sub> O <sub>x</sub> )	Simulated seawater	Nanopowder	Visible light	--	Rh <sub>2-y</sub> Cr <sub>y</sub> O <sub>3</sub>	333	[7]
p-GaN-InGaN	Natural seawater	Nanocomposite	AM 1.5	--	Rh/Cr <sub>2</sub> O <sub>3</sub>	50,960	[8]

**Table S2.** Representative summary of ferroelectrics annealed under reducing atmospheres

<b>Catalysts</b>	<b>Processing</b>	<b>Applications</b>	<b>Ref.</b>
SrBi <sub>2</sub> Ta <sub>2-x</sub> Nb <sub>x</sub> O <sub>9</sub>	H <sub>2</sub> annealing	Ferroelectric capacitor	[9]
SrTiO <sub>3</sub>	H <sub>2</sub> /N <sub>2</sub> annealing	--	[10]
Sr <sub>0.5</sub> Ba <sub>0.5</sub> TNb <sub>2</sub> O <sub>6</sub>	H <sub>2</sub> annealing	Piezocatalytic dye degradation	[11]
ZnSnO <sub>3</sub>	H <sub>2</sub> annealing	Piezocatalytic HER	[12]
BaTiO <sub>3</sub>	H <sub>2</sub> annealing	Piezocatalytic dye degradation	[13]
Na <sub>0.5</sub> Bi <sub>0.5</sub> TiO <sub>3</sub>	Vacuum Annealing	Piezocatalytic dye degradation	[14]
BiFeO <sub>3</sub>	Ar annealing	Photocatalytic dye degradation	[15]

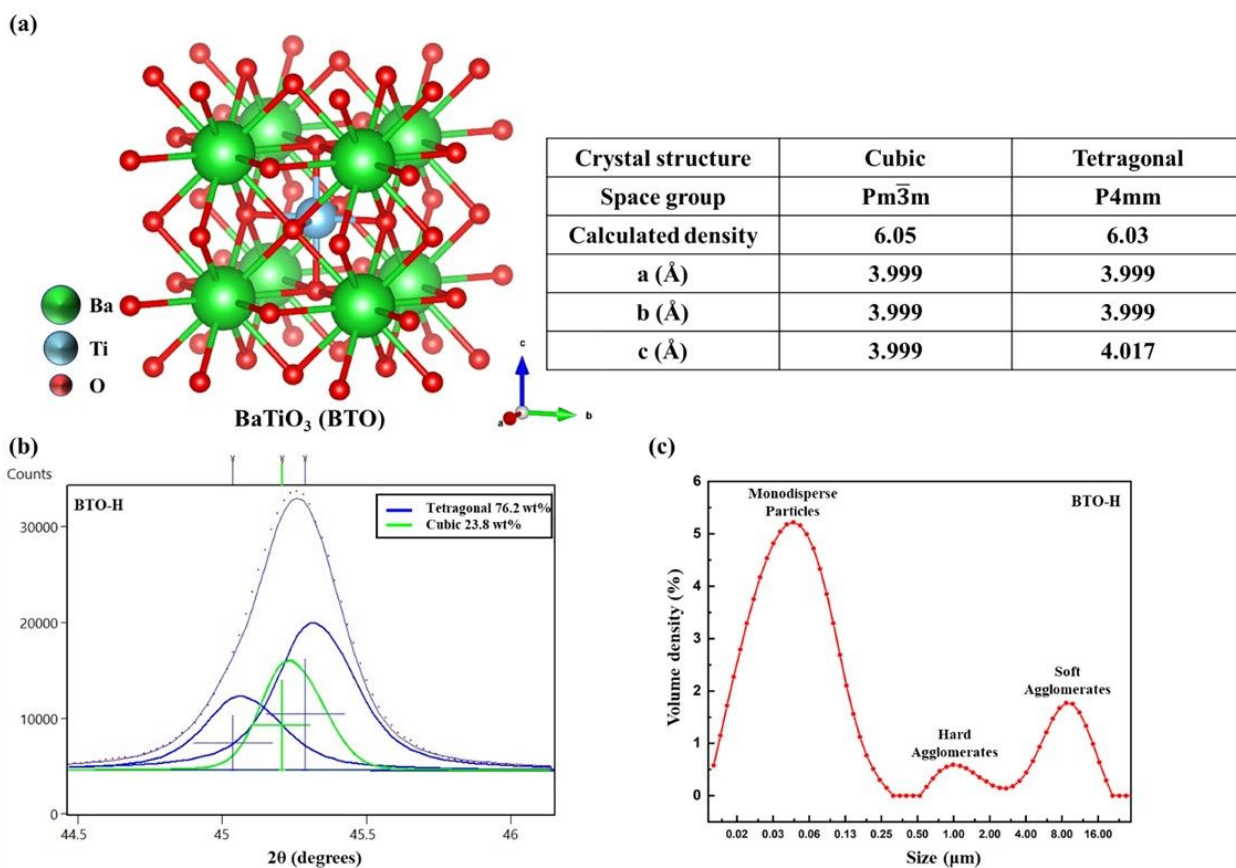


**Figure S1.** (a) Crystal structures and representative lattice parameter of cubic and tetragonal BaTiO<sub>3</sub> (visualized with VESTA 4.6.0 based on Crystallography Open Database), (b) XRD Rietveld refinement data for cubic and tetragonal BTO-H, (c) particle size distribution for cubic and tetragonal BTO-H obtained by laser diffraction (after sonication for 10 min)

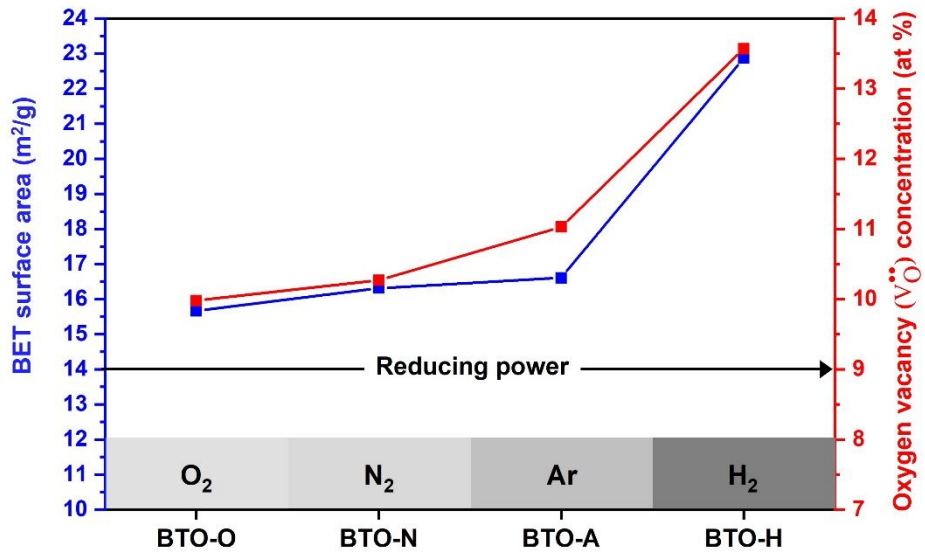


**Figure S2.** Correlation between BET surface area and oxygen vacancy concentration

**Table S3.** Brunauer-Emmett-Teller (BET) specific surface areas, pore volumes, and average pore sizes of defective BTO nanoparticles

<b>Sample</b>	<b>BTO-O</b>	<b>BTO-N</b>	<b>BTO-A</b>	<b>BTO-H</b>
<i>BET Specific Surface Area (m<sup>2</sup>/g)</i>	15.665	16.316	16.607	22.872
<i>Pore Volume (cm<sup>3</sup>/g)</i>	0.054	0.066	0.057	0.059
<i>Average Pore Size (nm)</i>	13.787	16.309	20.508	10.383

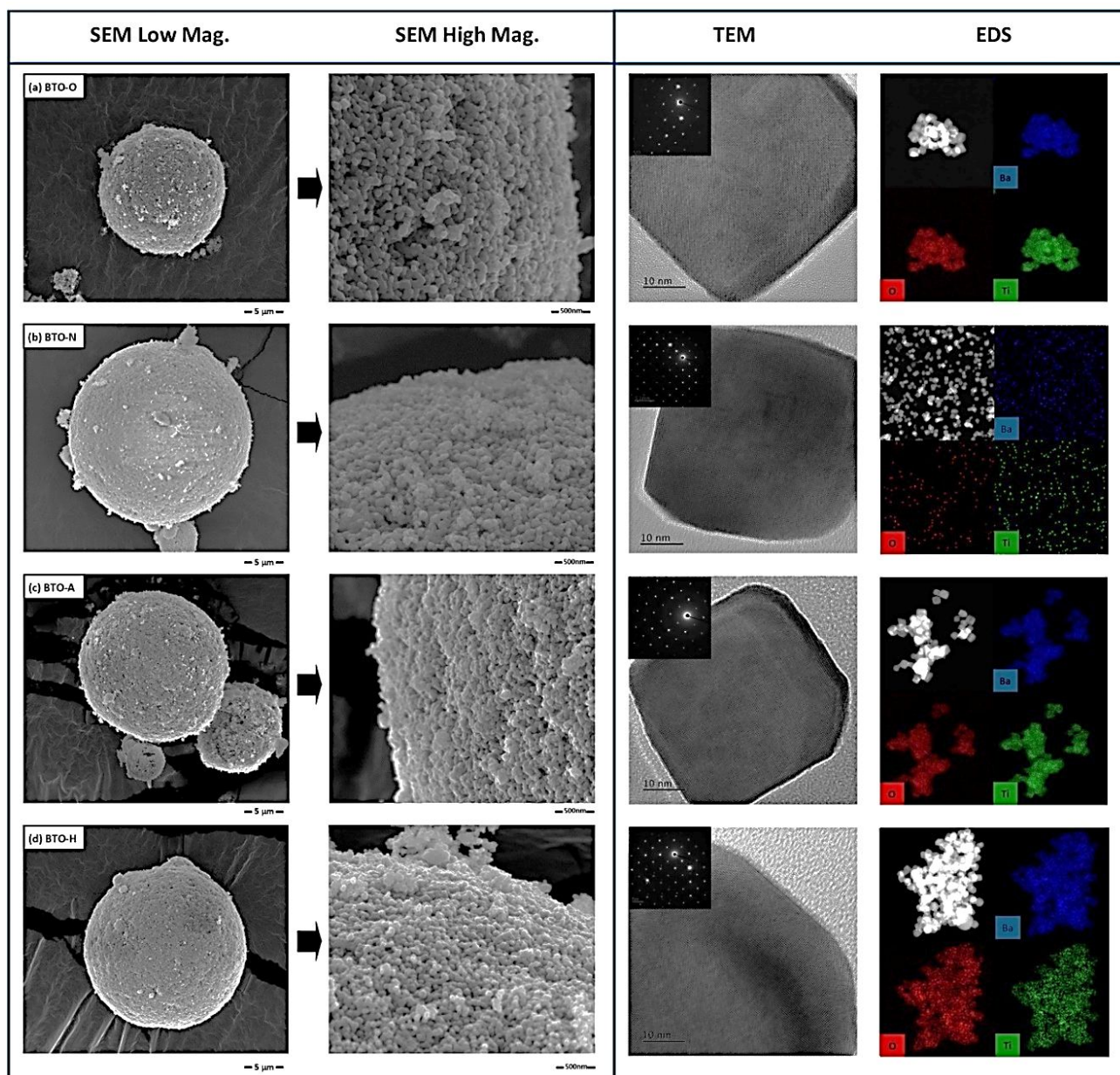


**Figure S3.** SEM, TEM, and EDS maps images of defective BTO nanoparticles: (a) BTO-O, (b) BTO-N, (c) BTO-A, (d) BTO-H (SEM before sonication; TEM images and EDS mapping after sonication)

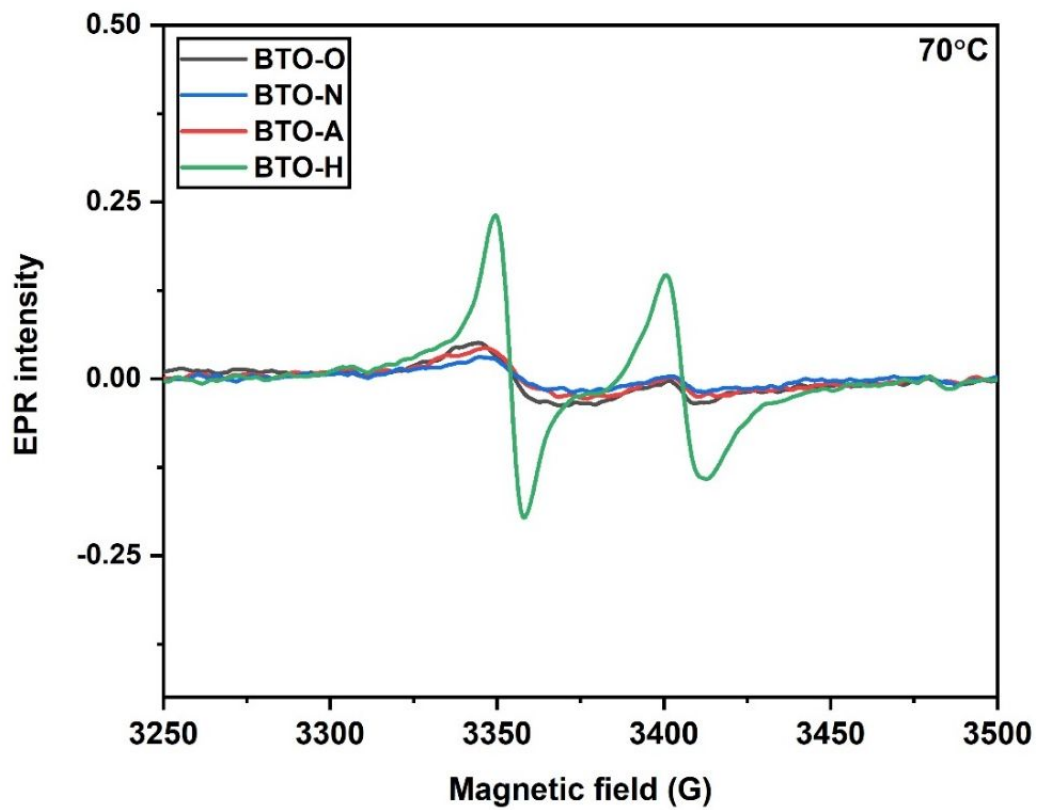


**Figure S4.** High-temperature (70°C in N<sub>2</sub>) EPR spectra of defective BTO nanoparticles

**Table S4.** Comparative analysis of XPS O1s peaks and calculated peak ratios for defective BTO nanoparticles

<b>XPS O1s peak</b>	<b>BTO-O [at%]</b>	<b>BTO-N [at%]</b>	<b>BTO-A [at%]</b>	<b>BTO-H [at%]</b>
O <sub>L</sub>	38.32	41.49	42.99	41.35
O <sub>V</sub>	4.25	4.75	5.33	6.49
O <sub>A</sub>	10.84	5.22	4.90	4.70
O <sub>V</sub> / O <sub>L</sub> + O <sub>V</sub>	9.98	10.27	11.03	13.57

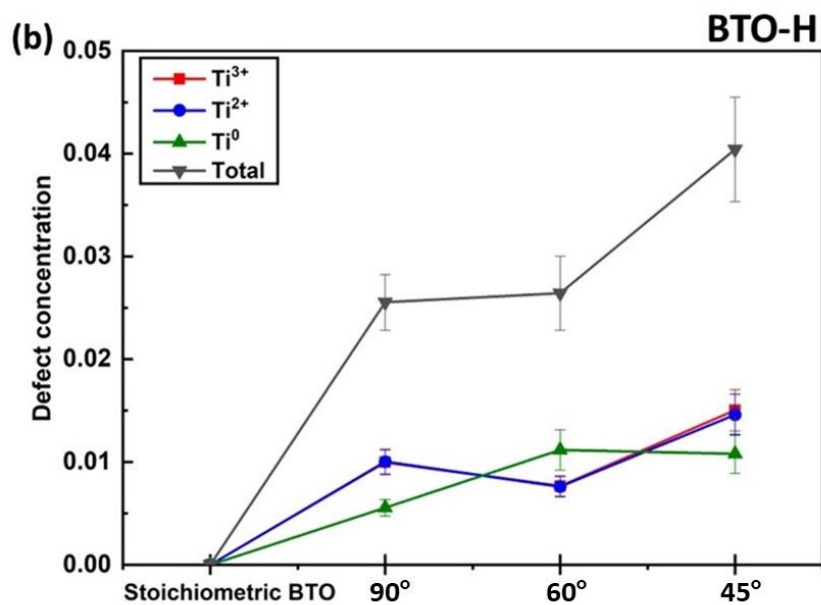
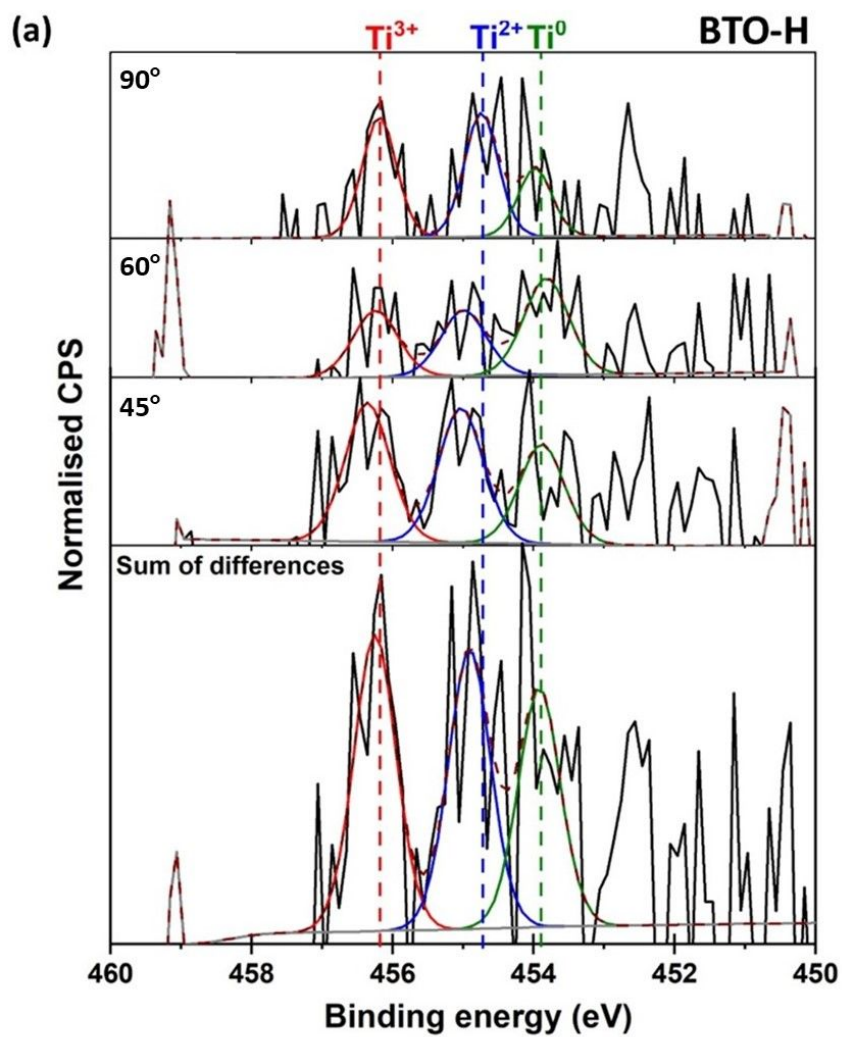


**Figure S5.** ARXPS Ti 2p spectra for BTO-H at beam angle relative sample surface: (a) Fitting relative to Ti<sup>4+</sup>, (b) Defect concentrations (error bars represent spread of reported values)

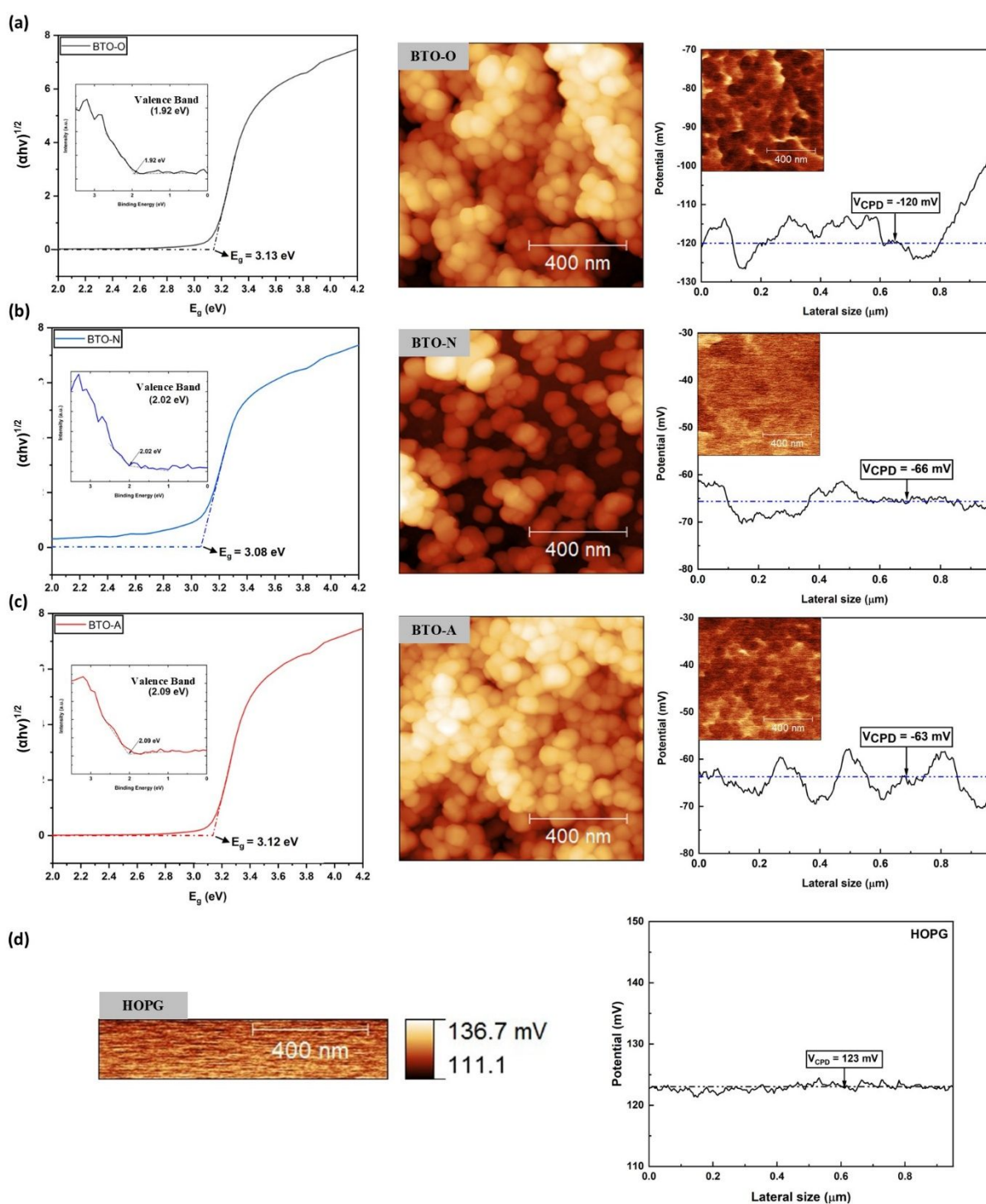


**Figure S6.** Kubelka-Munk plots from UV-Vis reflectance spectrophotometry data for optical indirect band gap, XPS valence band plots (inset) and topography and contact potential difference (CPD) obtained by KPFM imaging of defective BTO nanoparticles: (a) BTO-O, (b) BTO-N, (c) BTO-A, (d) freshly cleaved HOPG reference

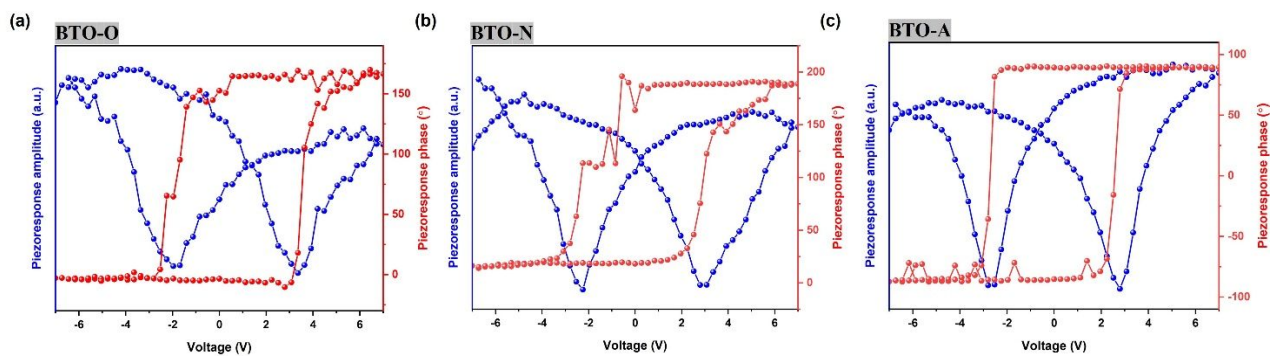


**Figure S7.** (a) PFM amplitudes and phase hysteresis loops of BTO-O, (b) PFM amplitudes and phase hysteresis loops of BTO-N, (c) PFM amplitudes and phase hysteresis loops of BTO-A

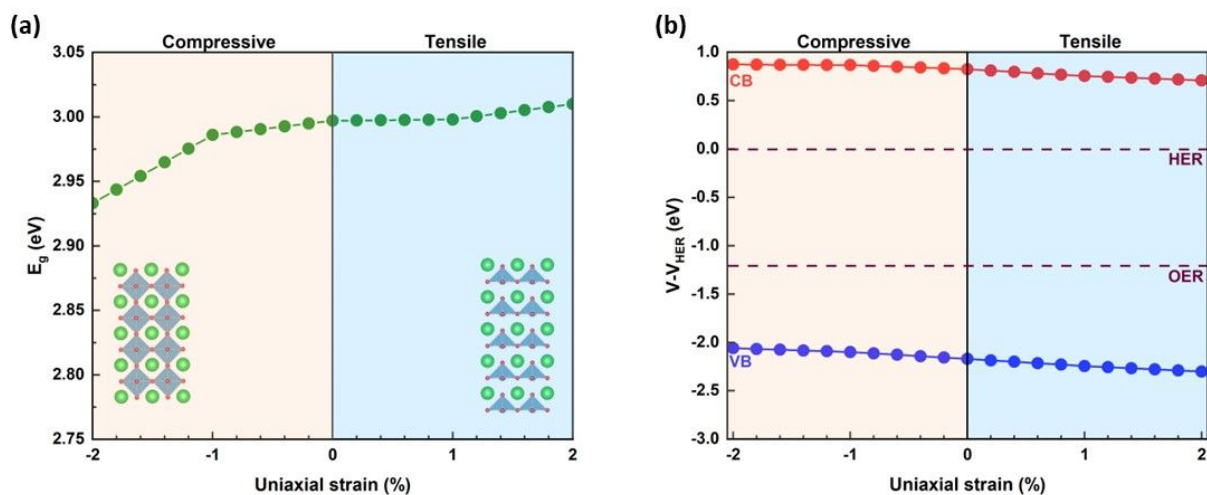


**Figure S8. DFT calculated band structure characteristics of defective BTO nanoparticles:** (a) Band gap change (ordinate scale range = 0.3 eV), (b) Band alignment change (ordinate scale range = 4.0 eV); external uniaxial strain range  $-2\%$  (compressive,  $\Delta c < 0$ ) to  $+2\%$  (tensile,  $\Delta c > 0$ ); strain level is commensurate with probable maximal lattice distortion imposed by ultrasound agitation.

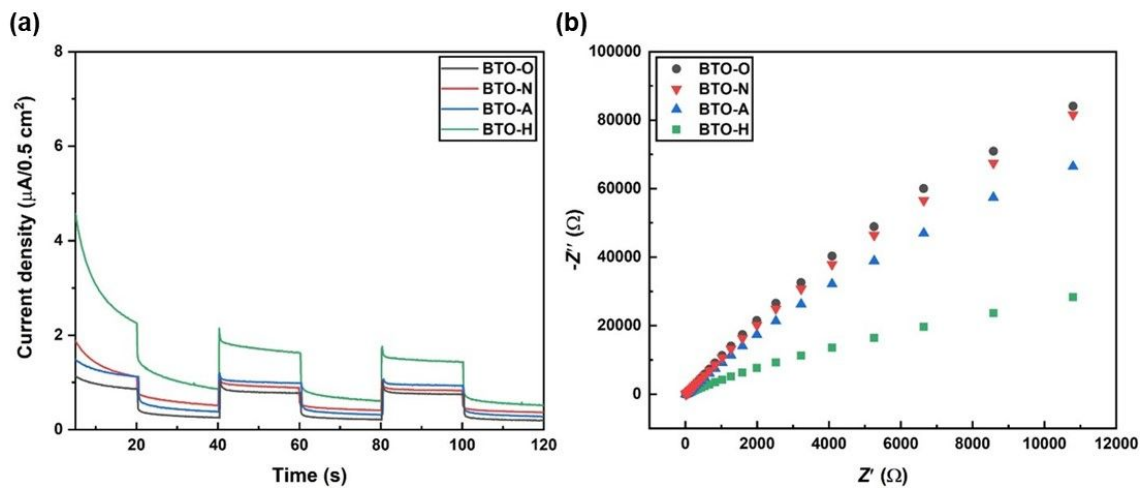


**Figure S9.** (a) Photoelectric current curves and (b) EIS curves of defective BTO nanoparticles

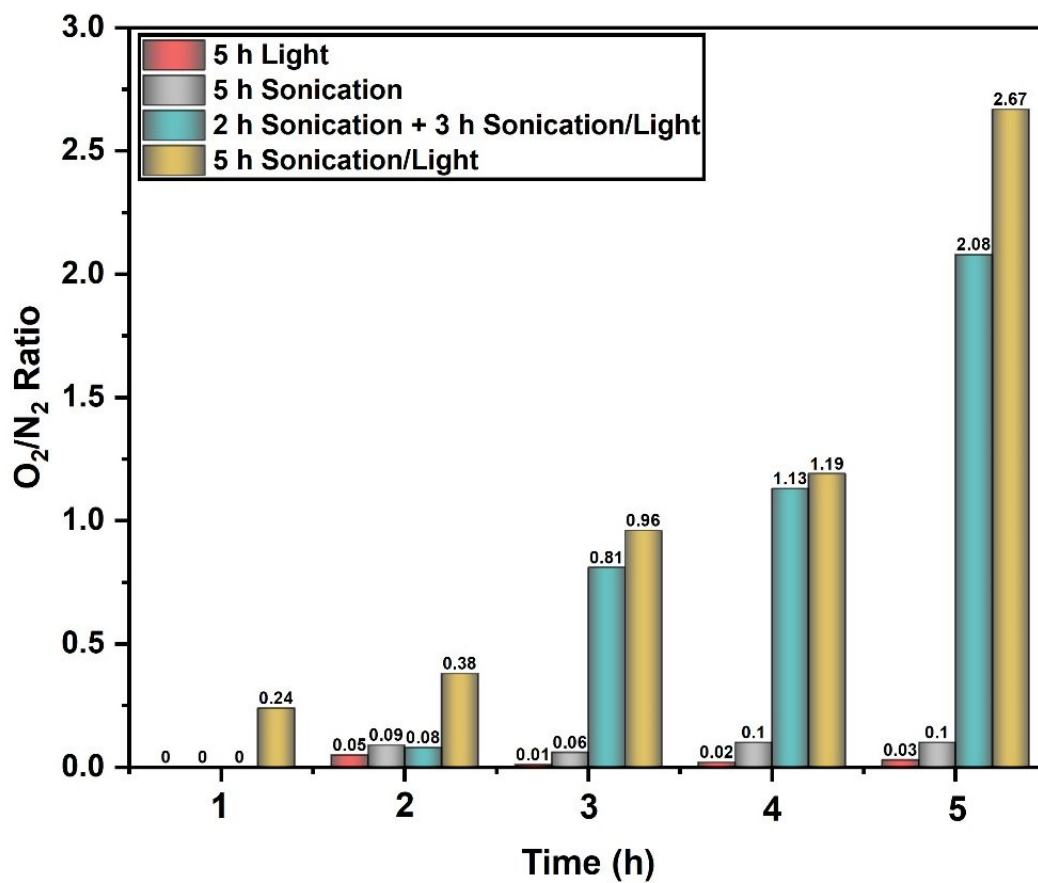


**Figure S10.** Measured O<sub>2</sub>/N<sub>2</sub> ratios in obtained mixed gas by GC under different test conditions

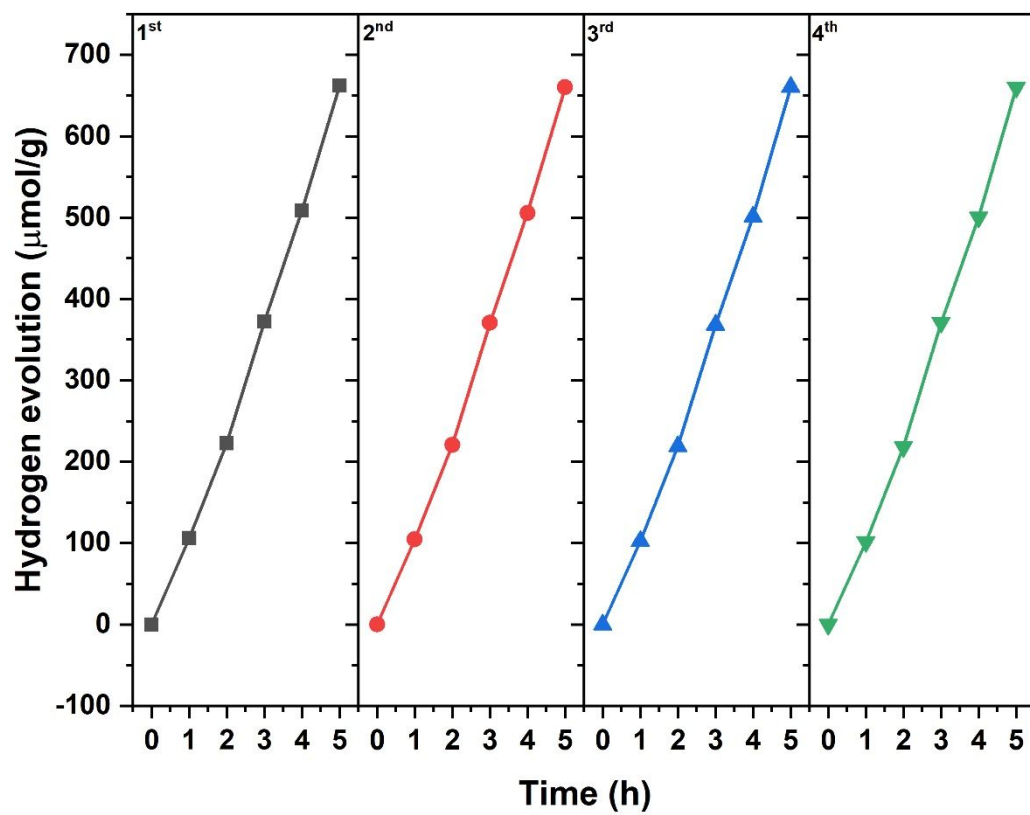


**Figure S11.** Recycling stability testing for piezo-photocatalytic HER performance of BTO-H

## Additional experimental analysis

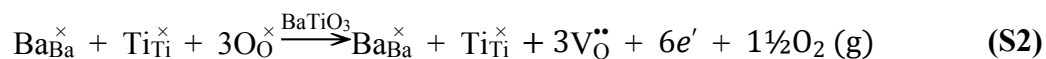
### Defect Equilibria

Only  $\text{Ti}^{3+}$  as the reductant is considered for the sake of simplicity.

Ionic Charge Compensation



Electronic Charge Compensation



Redox-Ionic Charge Compensation



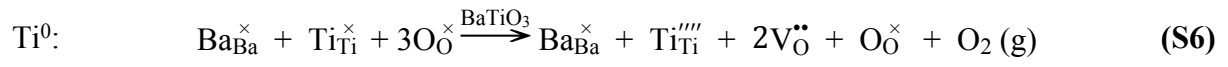
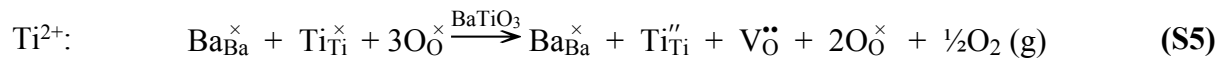
Redox-Electronic Charge Compensation



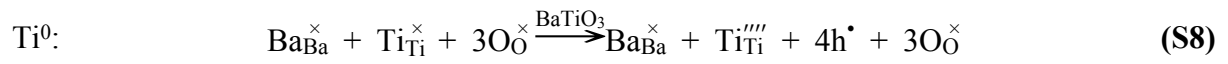
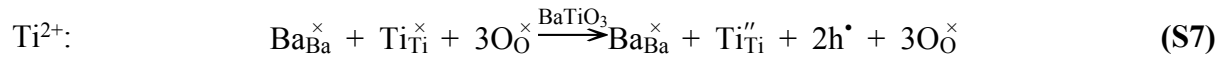
In terms of the formation of  $\text{V}_{\text{O}}^{\bullet\bullet}$ , **Equation S4** is anomalous in that reduction to form  $\text{V}_{\text{O}}^{\bullet\bullet}$  is absent but its presence would negate the necessity of charge compensation by  $h^{\bullet}$ . These potential defect equilibria demonstrate that neither ionic (**Equation S1**) nor electronic (**Equation S2**) charge compensation are possible because there is no Ti reduction. In contrast, both of the redox mechanisms are feasible because they include Ti reduction. That is, redox-ionic (**Equation S3**) combines ionic ( $\text{V}_{\text{O}}^{\bullet\bullet}$ ) and redox ( $\text{Ti}_{\text{Ti}}^{\prime}$ ) charge compensation and redox-electronic (**Equation S4**) combines electronic ( $h^{\bullet}$ ) and redox ( $\text{Ti}_{\text{Ti}}^{\prime}$ ) charge compensation.

The formation of oxygen vacancies is unambiguous as this is supported by the XRD, HAADF-STEM, BET, EPR, XPS, EELS, ARXPS, and PL data. Since electronic charge compensation does not involve oxygen vacancy formation, then the mechanism of charge compensation is redox-ionic (**Equation S3**). Thus, the representative defect equilibria representing the remaining reductions from  $\text{Ti}^{4+}$  in BTO to  $\text{Ti}^{2+}$  and  $\text{Ti}^0$  are:

Redox-Ionic Charge Compensation



Redox-Electronic Charge Compensation



## Energy Band Level Calculations

The CPD is defined as:

$$CPD = \Phi_{tip} - \Phi_{sample} \quad (S9)$$

where:

$$\begin{aligned} \Phi_{tip} &= \text{Work function of the metallic tip} \\ \Phi_{sample} &= \text{Work function of the sample surface} \end{aligned}$$

The work function of Si-coated tips is calibrated using highly ordered pyrolytic graphite (HOPG;  $\phi_{HOPG} = 4.6 \pm 0.1$  eV) [16] to convert the measured CPD to the absolute work function. The absolute surface work function of the sample is calculated as follows:

$$\Phi_{sample} = 4.6 \text{ eV} + CPD_{HOPG} - CPD_{sample} \quad (S10)$$

where:

$$\begin{aligned} CPD_{HOPG} &= \text{contact potential difference between the AFM tip and the HOPG reference} \\ CPD_{sample} &= \text{contact potential difference between the AFM tip and the sample} \end{aligned}$$

Since the measured  $CPD_{HOPG}$  and  $CPD_{BTO-H}$  were measured by 123 mV (**Figure S6**) and 107 mV (**Figure 4(b)**), respectively, then the work function for BTO-H is calculated as  $\sim 4.62$  eV [16]. The UV-Vis spectra for the optical indirect band gap calculation of BTO-H are shown in **Figure 4(d)**. The Kubelka-Munk method [17] was used to calculate the optical indirect band gap of 2.96 eV:

$$(F(R_{\infty})h\nu) = A(h\nu - E_g)^{1/2} \quad (S11)$$

where:

$$\begin{aligned} R_{\infty} &= \text{Relative diffuse reflectance} \\ h &= \text{Planck's constant} \\ \nu &= \text{Frequency} \\ A &= \text{Constant} \\ E_g &= \text{Optical indirect band gap} \end{aligned}$$

The XPS plot for the valence band edge ( $E_{VB}$ ) of BTO-H of 2.00 eV is shown in **Figure 4(e)**. On the basis of these data, the full energy band levels were calculated and a schematic of which is shown in **Figure 4(f)**.

The preceding data for the  $E_g$ ,  $E_{VB}$ , and  $V_{CPD}$  for BTO-O, BTO-N, and BTO-A are shown in **Figure S6**.

## DFT Simulations

First-principles calculations based on density functional theory (DFT) [18,19] were performed in order to simulate and analyze the influence of uniaxial strain,  $\eta$ , on the optoelectronic and band alignment properties of ferroelectric BaTiO<sub>3</sub> (tetragonal phase, space group  $P4mm$  [20]). The PBEsol functional [21] was used as implemented in the VASP software package [22]. The *projector augmented wave method* was used to represent the ionic cores by considering the most relevant electrons of each atomic species as the valence electrons. Wave functions were represented on a plane-wave basis truncated at 800 eV. For integrations within the Brillouin zone (BZ), Monkhorst-Pack k-point grids of spacing  $2\pi \times 0.01 \text{ \AA}^{-1}$  were used. Uniaxially strained bulk geometry relaxations were performed with a conjugate-gradient algorithm that allowed for volume variations while imposing the structural constraints defining uniaxial strain. Uniaxial strain was defined as  $\eta = (c-c_0)/c_0$ , where  $c_0$  represents the length of the unstrained lattice vector. Positive  $\eta$  values were considered tensile uniaxial strains and negative  $\eta$  were considered compressive. Periodic boundary conditions were applied along the three orthogonal directions defined by the lattice vectors. Consequently, possible surface effects were neglected in the bulk simulations (although not in the slab simulations, as described below). The relaxations were halted when all of the forces acting on the atoms were  $<0.005 \text{ eV} \cdot \text{\AA}^{-1}$ . Using these technical parameters, zero-temperature energies that were converged to within 0.5 meV per formula unit were obtained. Uniaxial strain conditions were simulated at  $\Delta\eta = 1\%$  intervals, which were used as the basis for linear fitting. In order to estimate accurate dielectric, piezoelectric, and band gap properties, the range-separated hybrid HSE06 exchange-correlation functional [23] was employed to perform single-point calculations on the equilibrium geometries determined at the PBEsol level.

To calculate accurate band alignments, the approach used by Moses *et al.* [24] for binary semiconductors was used. Briefly, both bulk and slab calculations were performed and these were used to determine the alignment of the electrostatic potential within the semiconductor material that could be obtained relative to the vacuum level. From the slab calculations, the difference between the average electrostatic potential within the semiconductor material and in vacuum was obtained. From the bulk calculations, the band structure shifts relative to the average electrostatic potential were determined.

These calculations were performed at each  $\eta$  point and these involved the estimation of macroscopic and planar average potentials. The planar potential was computed by averaging potential values within a well-defined plane (for example, perpendicular to the surface of the slab) and the macroscopic potential was obtained by taking the averages of the planar potentials over distances of one unit cell along a chosen direction. The slab systems were sufficiently thick to ensure that the electron density in the center of the slab was essentially equal to that of the bulk material. It was found that semiconductor slabs of 2.0-2.2 nm thickness accompanied by similarly large portions of vacuum provided sufficiently well converged results for the

electrostatic potentials. Band alignments (**Table S5**) were estimated systematically at the geometrical centers of adequately surface passivated BTO slabs.

**Table S5.** Energy band gaps and levels

Values	$E_g$ (eV)	$E_{CB}$ (eV)	$E_{VB}$ (eV)
<i>Experimental</i>	3.12	0.75	2.37
<i>Database</i>	2.99	0.83	2.17

**Figure S8(a)** shows the calculated  $\eta$  (strain) dependence of  $E_g$ . In the absence of strain, the computed value of 2.99 eV is in good agreement with present experimental measurement of 3.12 eV. It can be seen that  $E_g$  is only slightly increased under tension but it is reduced significantly under compression. This is interpreted in terms of the effect of direction on the tetragonality, where tension maintains the structure while compression shifts it toward pseudo-cubic. **Figure S8(b)** shows the CB and VB variations estimated for a point located at the center of the simulated BTO slab expressed as a function of uniaxial strain. Under tensile strain ( $\eta > 0$ ), both the CB and VB levels shift linearly toward lower potentials in a similar manner. These data suggest the presence of an internal electric field,  $E_{int}$ , which increases with  $\eta$  owing to an increasing accumulation of charges at the opposite surfaces. The accumulation of opposite charges derives from the piezoelectric effect (*i.e.*,  $E_{int} = Q/A\epsilon$ , where  $Q$  = polarization and piezoelectric surface charge,  $A$  = surface area,  $\epsilon$  = dielectric constant) and this produces significant band bending. Under compressive strain ( $\eta < 0$ ), the band bending mechanisms are same as under tension except that the potential shifts are of opposite direction (*i.e.*, the CB and VB levels shift towards higher potentials). However, the  $E_g$  reduction shown in **Figure S8(a)** for  $\eta < 0$  reveals differential trends in the CB, where the ascending variation is consistent with electrostatic effect of the internal electric field and the descending variation is consistent with the electronic effect of the  $E_g$ . Thus, under both compression and tension, the CB approaches the HER potential. In contrast, under compression, the VB approaches the OER potential but, under tension, it deviates away from the OER. However, the slope under tension is greater than that under compression, which is an important distinction as the sum of the two strain conditions during amplitude switching must be considered. These differential  $\eta$ -induced variations in the CB and VB potentials are consistent with overall enhancement of the HER by the CB trends, where both strain states cause approaches to the HER potential, and overall hindrance of the OER by the VB trends, where the greater slope under tension dominates the lower slope under compression.

## References

- [1] Simamora, A.J., Hsiung, T.L., Chang, F.C., Yang, T.C., Liao, C.Y. and Wang, H.P., Photocatalytic splitting of seawater and degradation of methylene blue on CuO/nano TiO<sub>2</sub>. *Int. J. Hydrog. Energy*, 2012, **37**(18), 13855-13858, <https://doi.org/10.1016/j.ijhydene.2012.04.091>.
- [2] Gao, M.M.; Connor, P.K.N. and Ho, G.W., Plasmonic photothermic directed broadband sunlight harnessing for seawater catalysis and desalination. *Energy Environ. Sci.* 2016, **9**, 3151–3160, <https://doi.org/10.1039/C6EE00971A>.
- [3] Ji, S.M., Jun, H., Jang, J.S., Son, H.C., Borse, P.H. and Lee, J.S., Photocatalytic hydrogen production from natural seawater. *J. Photochem. Photobiol. A Chem.*, 2007, **189**(1), 141-144, <https://doi.org/10.1016/j.jphotochem.2007.01.011>.
- [4] Qiu, B., Zhu, Q., Xing, M. and Zhang, J., A robust and efficient catalyst of Cd<sub>x</sub>Zn<sub>1-x</sub>Se motivated by CoP for photocatalytic hydrogen evolution under sunlight irradiation. *Chem. Commun.*, 2017, **53**(5), 897-900, <https://doi.org/10.1039/C6CC08311K>.
- [5] Li, Y.X.; He, F.; Peng, S.Q.; Lu, G.X. and Li, S.B. Photocatalytic H<sub>2</sub> evolution from NaCl saltwater over ZnS<sub>1-x-0.5y</sub>O<sub>x</sub>(OH)<sub>y</sub>-ZnO under visible light irradiation. *Int. J. Hydrog. Energy*, 2011, **36**, 10565–10573, <https://doi.org/10.1016/j.ijhydene.2011.05.166>.
- [6] Zhu, C., Liu, C.A., Fu, Y., Gao, J., Huang, H., Liu, Y. and Kang, Z., Construction of CDs/CdS photocatalysts for stable and efficient hydrogen production in water and seawater. *Appl. Catal. B Environ.*, 2019, **242**, 178-185, <https://doi.org/10.1016/j.apcatb.2018.09.096>.
- [7] Maeda, K., Masuda, H. and Domen, K., Effect of electrolyte addition on activity of (Ga<sub>1-x</sub>Zn<sub>x</sub>)(N<sub>1-x</sub>O<sub>x</sub>) photocatalyst for overall water splitting under visible light. *Catal. Today*, 2009, **147**(3-4), 173-178, <https://doi.org/10.1016/j.cattod.2008.09.002>.
- [8] Guan, X., Chowdhury, F.A., Pant, N., Guo, L., Vayssieres, L. and Mi, Z., Efficient unassisted overall photocatalytic seawater splitting on GaN-based nanowire arrays. *J. Phys. Chem. C*, 2018, **122**(25), 13797-13802, <https://doi.org/10.1021/acs.jpcc.8b00875>.
- [9] Cuchiaro, A.F.D. (2000). Compositional Dependence of Electrical Characteristics in SrBi<sub>2</sub>Ta<sub>2-x</sub>Nb<sub>x</sub>O<sub>9</sub> Ferroelectric Capacitor Reduced by H<sub>2</sub> Annealing. *Japanese Journal of Applied Physics*, **39**(4B), L371.
- [10] Lee, S., Yang, G., Wilke, R.H., Trolrier-McKinstry, S. and Randall, C.A. (2009). Thermopower in highly reduced n-type ferroelectric and related perovskite oxides and the role of heterogeneous nonstoichiometry. *Physical Review B*, **79**(13), 134110.
- [11] Dai, J., Shao, N., Zhang, S., Zhao, Z., Long, Y., Zhao, S. and Liu, W. (2021). Enhanced piezocatalytic activity of Sr<sub>0.5</sub>Ba<sub>0.5</sub>Nb<sub>2</sub>O<sub>6</sub> nanostructures by engineering surface oxygen vacancies and self-generated heterojunctions. *ACS Applied Materials & Interfaces*, **13**(6), 7259-7267.
- [12] Wang, Y.C. and Wu, J.M. (2020). Effect of controlled oxygen vacancy on H<sub>2</sub>-production through the piezocatalysis and piezophotonics of ferroelectric R3C ZnSnO<sub>3</sub> nanowires. *Advanced Functional Materials*, **30**(5), 1907619.
- [13] Ji, M., Kim, J.H., Ryu, C.H. and Lee, Y.I. (2022) Synthesis of self-modified black BaTiO<sub>3-x</sub> nanoparticles and effect of oxygen vacancy for the expansion of piezocatalytic application. *Nano Energy*, **95**, 106993
- [14] Liu, D.M., Zhang, J.T., Jin, C.C., Chen, B.B., Hu, J., Zhu, R. and Wang, F. (2022). Insight into oxygen-vacancy regulation on piezocatalytic activity of (Bi<sub>1/2</sub>Na<sub>1/2</sub>)TiO<sub>3</sub> crystallites: Experiments and first-principles calculations. *Nano Energy*, **95**, 106975.
- [15] Wang, W., Li, N., Chi, Y., Li, Y., Yan, W., Li, X. and Shao, C. (2013). Electrospinning of magnetical bismuth ferrite nanofibers with photocatalytic activity. *Ceramics International*, **39**(4), 3511-3518.

- [16] Melitz, W., Shen, J., Lee, S., Lee, J.S., Kummel, A.C., Droopad, R. and Yu, E.T., Scanning tunneling spectroscopy and Kelvin probe force microscopy investigation of Fermi energy level pinning mechanism on InAs and InGaAs clean surfaces. *J. Appl. Phys.*, 2010, **108**(2), 023711, <https://doi.org/10.1063/1.3462440>.
- [17] Kortüm, G., Braun, W. and Herzog, G., Principles and techniques of diffuse-reflectance spectroscopy. *Angew. Chem.*, 1963, **2**(7), pp.333-341, <https://doi.org/10.1002/anie.196303331>.
- [18] Cazorla, C. The role of density functional theory methods in the prediction of nanostructured gas-adsorbent materials. *Coord. Chem. Rev.* 2015, **300**, 142, <https://doi.org/10.1016/j.ccr.2015.05.002>.
- [19] Cazorla, C. and Boronat, B., Simulation and understanding of atomic and molecular quantum crystals. *Rev. Mod. Phys.* 2017, **89**, 035003, <https://doi.org/10.1103/RevModPhys.89.035003>.
- [20] Brutchey, R.L. and Morse, D.E., Template-free, low-temperature synthesis of crystalline barium titanate nanoparticles under bio-inspired conditions. *Angew. Chem.* 2006, **118**(39), 6714-6716, <https://doi.org/10.1002/ange.200602571>.
- [21] Perdew, J.P., Ruzsinszky, A., Csonka, G.I., Vydrov, O.A., Scuseria, G.E., Constantin, L.A., Zhou, X., and Burke, K. Restoring the density-gradient expansion for exchange in solids and surfaces. *Phys. Rev. Lett.* 2008, **100**, 136406, <https://doi.org/10.1103/PhysRevLett.100.136406>.
- [22] Kresse, G. and Fürthmüller, J., Efficient iterative schemes for ab initio total-energy calculations using a plane-wave basis set. *Phys. Rev. B*, 1996, **54**, 11169, <https://doi.org/10.1103/PhysRevB.54.11169>.
- [23] Krukau, A.V., Vydrov, O.A., Izmaylov, A.F. and Scuseria, G.E., Influence of the exchange screening parameter on the performance of screened hybrid functionals. *J. Chem. Phys.* 2006, **125**, 224106, <https://doi.org/10.1063/1.2404663>.
- [24] Moses, P. G., Miao, M., Yan, Q. and Van de Walle, C.G., Hybrid functional investigations of band gaps and band alignments for AlN, GaN, InN, and InGaN. *J. Chem. Phys.* 2011, **134**, 084703, <https://doi.org/10.1063/1.3548872>.